

Relation between the properties of the kilohertz quasi-periodic oscillations and spectral parameters in 4U 1636–53.

Evandro M. Ribeiro¹★, Mariano Méndez¹, Guobao Zhang², and Andrea Sanna³

¹*Kapteyn Astronomical Institute, University of Groningen, P.O. BOX 800, 9700 AV Groningen, The Netherlands*

²*New York University Abu Dhabi, P.O. Box 129188, Abu Dhabi, United Arab Emirates*

³*Dipartimento di Fisica, Università degli Studi di Cagliari, SP Monserrato-Sestu km 0.7, I-09042, Monserrato, Italy*

Accepted XXX. Received YYY; in original form ZZZ

ABSTRACT

We investigate the relation between the parameters of the energy spectrum and the frequency and amplitude of the kilohertz quasi-periodic oscillations (kHz QPOs) in the low-mass X-ray binary 4U 1636–53. We fit the 3–180-keV spectrum of this source with a model that includes a thermal Comptonisation component. We show that the frequencies of both kHz QPOs follow the same relation as a function of the parameters of this spectral component, except for a systematic frequency shift, whereas the rms fractional amplitude of each QPO follows a different relation with respect to those same parameters. This implies that, while the dynamical mechanism that sets the frequencies of the QPO can be the same for both kHz QPOs, the radiative mechanisms that set the amplitudes of the lower and the upper kHz QPO are likely different. We discuss the implications of these results to the modelling of the kHz QPOs and the possibility that the lower kHz QPO reflects a resonance between the Comptonising medium and the photons from the accretion disc and/or the neutron star surface.

Key words: accretion, accretion discs – stars: neutron – X-rays: binaries – stars: individual: 4U 1636–53

1 INTRODUCTION

The spectral and timing properties of neutron star low-mass X-ray binaries (NS-LMXB) depend upon the position of the source in the so called colour-colour diagram (CD; e.g., [Hasinger & van der Klis 1989](#)). For NS-LMXB the position of the source in the CD can be described by a single parameter, S_a (e.g., [Kuulkers et al. 1994](#); [Méndez et al. 1999](#)). The characteristic frequencies observed in the power density spectra (PDS) of these sources are correlated with S_a (e.g., [Méndez et al. 1999](#); [Van Straaten et al. 2000](#); [Di Salvo et al. 2001, 2003](#)). A typical example is the central frequency of one of the kilohertz quasi-periodic oscillation (kHz QPO), specifically the upper kHz QPO, which is positively correlated with S_a ([Méndez et al. 1999](#); [Belloni et al. 2005, 2007](#); [Sanna et al. 2012](#)).

[Hasinger & van der Klis \(1989\)](#) proposed that the evolution of the source in the CD is driven by changes in the mass accretion rate in the system and it is often considered a better tracer of accretion rate than X-ray luminosity (e.g., [Kuulkers et al. 1994](#); [Jonker et al. 1998](#); [Méndez et al. 1999](#);

[Ford et al. 2000](#); [Van Straaten et al. 2000](#); [Méndez et al. 2001](#)). As the accretion rate increases the source spectrum softens due to the increase of the relative contribution of the accretion disc and the neutron star surface to the total emission, and the more efficient cooling of the corona. At the same time, the truncation radius decreases ([Done et al. 2007](#)) and the temperature at the inner edge of the disc increases. This scenario is consistent with the correlation between the upper kHz QPO frequency and S_a , if this QPO reflects the orbital frequency of matter at the inner edge of the disc ([Miller et al. 1998](#); [Stella & Vietri 1998](#)). The lower kHz QPO appears only within a narrow range of S_a (e.g., [Zhang et al. 2017](#)), and hence a correlation with S_a is unclear.

4U 1636–53 is an LMXB with an orbital period of 3.8 h ([Van Paradijs et al. 1990](#)) and the accreting neutron star has a spin rate of 581 Hz ([Zhang et al. 1997](#)). This source shows a cycle of ~ 40 days ([Shih et al. 2005](#)) during which it evolves through different spectral states covering the full CD. This makes it an exceptional target to explore the relation between its timing and spectral properties.

[Zhang et al. \(2017\)](#) recently studied the relation between the presence of the kHz QPO and the spectral evolu-

★ E-mail: ribeiro@astro.rug.nl

tion of the source in the NS-LMXB 4U 1636–53. Based on their results, here we study the relation between the properties of the kHz QPO and the spectral properties of this source to gain insight on the mechanism that drives the appearance of the kHz QPOs. In §2 we describe the dataset, models and methods used, in §3 we show our results and, finally, we discuss these results and summarise our findings in §4

2 OBSERVATIONS AND DATA ANALYSIS

For this work we use all 1576 observations of the NS-LMXB 4U 1636–53 taken with the Rossi X-ray Timing Explorer (*RXTE*) Proportional Counter Array (PCA; [Jahoda et al. 2006](#)) and the High-Energy X-ray Timing Experiment (HEXTE; [Rothschild et al. 1998](#)).

2.1 Timing Analysis

We produced Fourier PDS using the event-mode data with a time resolution of 125 μ s covering the full PCA energy band. We set the sample rate to 1/4096 s, which yields a Nyquist frequency of 2048 Hz, and calculated a PDS every 16 s; we finally averaged all 16-s PDS of each observation to yield a single PDS per observation.

We ignored frequencies below 200 Hz and fitted a Lorentzian to each possible QPO in the average PDS of each observation using the same criteria as [Sanna et al. \(2012\)](#), which was to accept all QPOs where the ratio between the Lorentzian normalisation and its negative 1σ error was larger than 3, and the coherence, Q , was larger than 2, where Q is the ratio between the central frequency and the FWHM of the Lorentzian. When only one kHz QPO was detected we identified it as upper or lower kHz QPO based on the branches of the diagram of QPO frequency vs. S_a (see, for example, Figure 1 in [Sanna et al. 2012](#)). We detected kHz QPOs in 581 out of 1576 observations; we detected the lower kHz QPO in 403 and the upper in 206 of those observations.

We then combined the data by averaging the PDS of observations where the mean QPO frequency belongs to the frequency ranges shown in [Table 1](#), for the lower and upper kHz QPO, respectively. The choice of these frequency ranges was made to allow an approximately equal number of power spectra per frequency range, except for the two lowest frequency ranges of the lower kHz QPO, for which there are only a handful of observations available. We did not apply any shift-and-add procedure ([Méndez et al. 1998](#)) to combine the power spectra.

For each of the frequency ranges of the lower (upper) QPO we searched the averaged PDS for the corresponding upper (lower) QPO. This allowed us to recover one of the kHz QPOs from the averaged PDS even if that QPO was not significantly detected in each individual observation.

For each frequency interval of the QPOs we estimated the average background contribution to the PCA lightcurve using the `ftool` `RUNPCABACKEST`, and we used this background count rate, together with that of the source, to calculate the rms amplitude of the QPOs for each selection.

2.2 Spectral Analysis

For the spectral properties of the source within each frequency interval we used the results from [Zhang et al. \(2017\)](#). To get these parameters [Zhang et al. \(2017\)](#) fitted the PCA and HEXTE spectra of 4U 1636–53 using the package `XSPEC v12.7` ([Arnaud 1996](#)). To account for interstellar absorption they used the model component `PHABS` with cross-sections from [Balucinska-Church & McCammon \(1992\)](#) and solar abundances from [Anders & Grevesse \(1989\)](#), fixing the column density to $N_{\text{H}} = 3.1 \times 10^{21} \text{ cm}^{-2}$ ([Sanna et al. 2013](#)). [Zhang et al. \(2017\)](#) added a multiplicative factor to account for calibration uncertainties between the PCA and HEXTE instruments.

The continuum emission of the source was fitted with a model consisting of a multi-colour disc blackbody (`DISKBB` model, [Mitsuda et al. 1984](#); [Makishima et al. 1986](#)), a single temperature blackbody (`BODYRAD`) and a Comptonisation model (`NTHCOMP`, [Zdziarski et al. 1996](#); [Życki et al. 1999](#)) to describe, respectively, the emission from the disc, the NS surface (or boundary layer), and the Comptonised component. [Zhang et al. \(2017\)](#) included a Gaussian component with a variable width in the model to account for the presence of an iron line; the energy of the line was fixed to 6.5 keV. The temperature of the disc blackbody at the inner disc radius (kT_{dbb}) was interpolated along the colour-colour diagram using the joint XMM Newton–*RXTE* spectral fitting results in [Sanna et al. \(2013\)](#) and set to 0.3, 0.2, 0.4, 0.45, 0.6, 0.75 and 0.8 keV for S_a equal to 1.1, 1.3, 1.5, 1.7, 1.9, 2.1, and 2.35, respectively. They left the temperature of the `BODYRAD` component free during the fits.

Further details on the spectral models and the fitting results are given in [Zhang et al. \(2017\)](#). Those authors explored in depth the modelling and interpretation of the X-ray spectra of 4U 1636–53 and their relation to the presence of the lower kHz QPO. For this work we use the spectral parameters found by [Zhang et al. \(2017\)](#) to represent the best-fitting model for each observation.

From the Comptonisation model, assuming a spherically symmetric region, the asymptotic power-law photon index, Γ , can be expressed as:

$$\Gamma = \left[\frac{9}{4} + \frac{1}{(kT_e/m_e c^2)\tau(1 + \tau/3)} \right]^{1/2} - \frac{1}{2}, \quad (1)$$

where τ is the optical depth of the region, and kT_e is the electron temperature ([Sunyaev & Titarchuk 1980](#)). Both Γ and kT_e are obtained from the best fitting model, and are used to calculate the optical depth τ from [Equation 1](#).

We excluded observations with power-law index $\Gamma < 1.2$ for the averaging of spectral parameters, as that is close to the lower boundary of the allowed parameter values ($\Gamma = 1$) and represents a possible unconstrained fit ([Zhang et al. 2017](#)). That left us with a total of 558 observations, containing 385 observations with a lower kHz QPO and 201 with an upper kHz QPO.

In order to parameterize the spectral evolution of the source we extracted the PCA lightcurves in 4 energy-bands, following [Zhang et al. \(2017\)](#), to create a colour-colour diagram ([Fig. 1](#)). The hard and soft colours were defined as the count rate ratio between the energy bands 9.7–16.0/6.0–9.7

Table 1. Overview of the selection by QPO frequencies used in this work and, for each frequency interval, the average spectral parameters taken from Zhang et al. (2017), and the fractional rms amplitude of the QPO. The numbers in between parentheses represent the number of observations used to investigate timing-only properties, before excluding the ones with low values of Γ (see text). Uncertainties in the rms fractional amplitude represent the 1σ confidence interval obtained from the best fit to the combined power spectra. Uncertainties in the other variables represent the 1σ error of the mean in each averaged interval.

Lower kHz QPO							
Frequency range (Hz)	Number of observations	Average frequency (Hz)	S_a	Γ	kT_e (keV)	τ	rms (%)
470–590	4	562.1 ± 8.4	2.013 ± 0.039	2.13 ± 0.04	4.26 ± 0.46	7.6 ± 0.7	4.27 ± 0.30
590–620	4	608.1 ± 6.3	2.000 ± 0.013	2.12 ± 0.07	4.79 ± 0.49	7.1 ± 0.6	4.49 ± 0.50
620–670	28 (30)	648.1 ± 2.3	2.060 ± 0.005	2.13 ± 0.05	4.64 ± 0.30	7.8 ± 0.6	6.55 ± 0.15
670–715	35 (38)	696.6 ± 2.1	2.093 ± 0.005	2.05 ± 0.04	3.86 ± 0.13	9.1 ± 0.7	7.56 ± 0.14
715–750	36 (37)	733.0 ± 2.0	2.096 ± 0.004	2.07 ± 0.05	3.68 ± 0.13	9.4 ± 0.7	7.95 ± 0.13
750–790	39 (42)	766.8 ± 1.7	2.111 ± 0.004	1.98 ± 0.04	3.21 ± 0.08	10.3 ± 0.4	7.62 ± 0.10
790–820	40 (42)	806.6 ± 1.2	2.118 ± 0.005	1.90 ± 0.04	3.09 ± 0.09	11.2 ± 0.5	7.74 ± 0.09
820–850	45 (46)	834.5 ± 1.5	2.133 ± 0.005	1.93 ± 0.03	3.03 ± 0.07	10.9 ± 0.4	7.65 ± 0.06
850–880	55 (59)	864.1 ± 1.2	2.134 ± 0.004	1.81 ± 0.03	2.81 ± 0.04	12.4 ± 0.4	6.57 ± 0.05
880–910	55 (57)	895.7 ± 1.2	2.142 ± 0.005	1.77 ± 0.03	2.78 ± 0.03	13.1 ± 0.5	5.48 ± 0.06
910–975	44	922.5 ± 1.3	2.149 ± 0.004	1.81 ± 0.03	2.85 ± 0.05	12.4 ± 0.4	3.98 ± 0.08
Upper kHz QPO							
Frequency range (Hz)	Number of observations	Average frequency (Hz)	S_a	Γ	kT_e (keV)	τ	rms (%)
440–540	12	490.2 ± 9.8	1.336 ± 0.022	1.80 ± 0.01	9.53 ± 0.34	6.0 ± 0.2	13.5 ± 0.7
540–650	27	607.4 ± 4.9	1.509 ± 0.017	1.90 ± 0.01	12.28 ± 2.47	5.5 ± 0.3	11.9 ± 0.5
650–750	32	704.9 ± 4.2	1.710 ± 0.009	2.01 ± 0.02	10.46 ± 2.01	5.5 ± 0.2	11.5 ± 0.3
750–810	42	783.0 ± 2.4	1.837 ± 0.006	2.14 ± 0.02	10.13 ± 1.82	5.3 ± 0.2	11.4 ± 0.2
810–870	28	839.5 ± 3.4	1.918 ± 0.005	2.17 ± 0.02	7.03 ± 0.79	5.9 ± 0.3	10.5 ± 0.2
870–930	18 (20)	896.5 ± 4.4	1.989 ± 0.006	2.19 ± 0.03	5.13 ± 0.38	6.7 ± 0.4	9.1 ± 0.2
930–1025	17	970.0 ± 6.6	2.054 ± 0.009	2.09 ± 0.06	4.34 ± 0.27	8.3 ± 0.9	6.5 ± 0.3
1025–1165	7	1127.5 ± 13.2	2.160 ± 0.015	1.79 ± 0.06	2.75 ± 0.03	12.6 ± 1.0	3.5 ± 0.3
1165–1250	18 (21)	1204.8 ± 4.3	2.194 ± 0.014	1.76 ± 0.05	2.79 ± 0.03	13.3 ± 1.0	2.6 ± 0.2

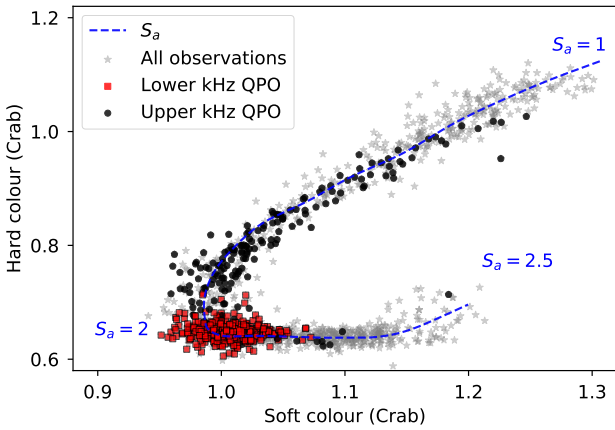


Figure 1. Colour-colour diagram of 4U 1636–53. Each point in this diagram represents a full RXTE/PCA observation. Red and black points represent observations with, respectively, a lower or an upper kHz QPO. (Observations with two simultaneous kHz QPOs are shown in red.) Grey points represent observations without kHz QPOs

keV and 3.5–6.0/2.0–3.5 keV, respectively, per observation. The parameterization, S_a , is defined by the length of the dashed-blue line in Fig. 1, fixing $S_a = 1$ at the top right position of the diagram and $S_a = 2$ at the bottom left position (e.g. Méndez et al. 1999).

3 RESULTS

For each of the frequency intervals of the QPO defined in Table 1, we computed the averaged spectral parameters of the source and we investigated the relation between these averaged parameters and the averaged QPO properties. In Fig. 2 we show the relation between averaged spectral parameters and the frequency of the kHz QPOs. In all panels red and black (grey and black in the printed version) symbols represent the lower and upper kHz QPO, respectively.

In the upper-left panel of Fig. 2 we show the power-law index, Γ , as a function of QPO frequency. It is apparent that Γ decreases from ~ 2.2 to ~ 1.8 as the frequency of the lower kHz QPO increases from ~ 500 Hz to ~ 900 Hz, while for the upper kHz QPO Γ first increases from ~ 1.8 to ~ 2.2 as the frequency of this QPO increases from ~ 500 Hz to ~ 850 Hz, and then decreases from ~ 2.2 to ~ 1.8 as the frequency of this QPO increases to approximately 1200 Hz.

In the middle-left panel of Fig. 2 we show the relation between the optical depth, τ , and the frequency of the kHz QPOs. This figure shows that τ increases from 6 to 14 as the frequency of the lower kHz QPO increases from ~ 500 Hz to ~ 900 Hz. As the frequency of the upper kHz QPO increases from 500 Hz to 850 Hz τ remains approximately constant between 5 and 6 and then increases to 14 as the frequency increases from 800 Hz to 1200 Hz.

On the bottom-left panel of Fig. 2 we show the electron temperature of the Comptonising region, kT_e , as a function of QPO frequency. The temperature remains approximately constant as the frequency of the lower kHz QPO increases from 500 Hz to 600 Hz and decreases slowly to 3 keV as

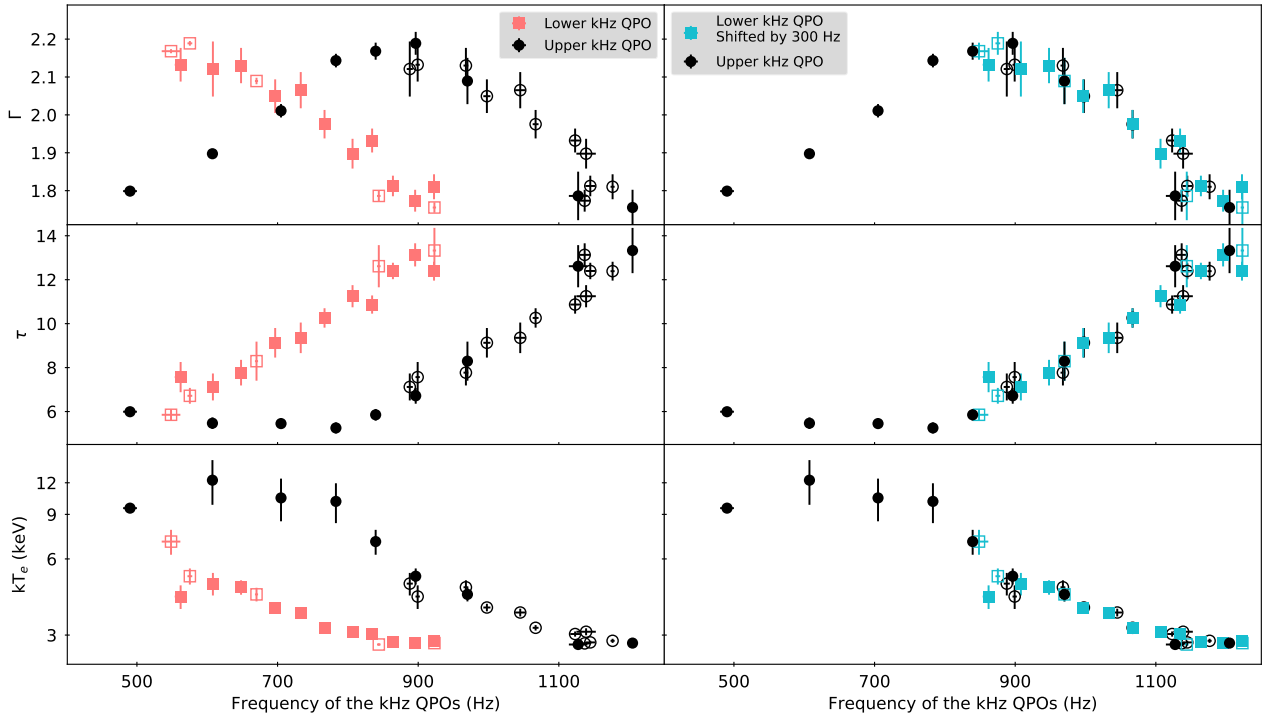


Figure 2. Relation between spectral parameters and kHz QPO frequency in 4U 1636–53. The data are the average in the frequency ranges given in section 2. For the plots on the right side the frequency of the lower kHz QPO was shifted by 300 Hz, which is close to the average separation between the twin kHz QPO (Jonker et al. 2002). The open black (red or blue) symbols (respectively black and grey in the printed version) correspond to the upper (lower) kHz QPO detected after combining the PDSs within the frequency ranges chosen for the lower (upper) kHz QPO. Error bars represent the 1σ error of the mean in each bin. The y axis is shown in \log scale in the two bottom panels for better visualisation.

the frequency increases to 900 Hz. As the frequency of the upper kHz QPO increases from 400 Hz to 600 Hz kT_e remains approximately constant, and then decreases slowly to 3 keV as the QPO frequency increases to 1200 Hz

The right-side panels of Fig. 2 reproduce the left-side plots but with the frequency of the lower kHz QPO shifted by 300 Hz, which is close to the average separation between the upper and lower kHz QPO frequencies (Jonker et al. 2002). These panels show that the relation between the spectral parameters and the frequency of the upper kHz QPO and the shifted lower kHz QPO can be described by a single relation, as expected due to the almost constant frequency separation between both kHz QPOs. These plots also show that the relations are valid for each QPO regardless of the presence of the other QPO.

In Fig. 3 we show the parameter S_a ¹ and the fractional rms amplitude of the QPOs as a function of τ and kT_e . In the top-left panel of Fig. 3 we show that as S_a increases from ~ 1.2 to ~ 1.8 the optical depth τ of the corona remains approximately constant, and then τ increases steeply as S_a increases from ~ 1.8 to ~ 2.2 . As noticed by Zhang et al. (2017) the lower kHz QPO is detected only when τ is larger

than ~ 6 and increases rapidly. The relation between S_a and electron temperature kT_e is shown in the top-right panel. As S_a increases from ~ 1.2 to ~ 1.8 the temperature is consistent with being constant within errors, and decreases abruptly as S_a increases from ~ 1.8 to ~ 2.2 . This trend is similar to the one in the top-left panel of this Figure, but one has to keep in mind that the optical depth is obtained from the fitted values of Γ and kT_e .

The bottom-left panel of Fig. 3 shows the fractional rms amplitude of both QPOs as a function of the optical depth τ of the Comptonising component. When τ is low (< 7) the amplitude of the upper kHz QPO is high ($> 10\%$) and the amplitude decreases to a minimum as τ increases to ~ 11 . The lower kHz QPO displays a very different trend with its rms amplitude increasing from $\sim 4\%$ to $\sim 8\%$ as τ increases from ~ 5 to ~ 11 , and then decreasing as τ continues increasing to ~ 14 .

We observe a similar trend in the bottom-right panel showing the relation of the rms amplitude of each QPO with the electron temperature of the Comptonising region. The amplitude of the upper kHz QPO is low ($\sim 4\%$) when the temperature is below 3 keV and it increases up to $\sim 14\%$ as the temperature raises to ~ 15 keV. Meanwhile the amplitude of the lower kHz QPO increases from 3% to 8% as the temperature increases from ~ 2.5 keV to ~ 3.5 keV and then decreases to $\sim 5\%$ as the temperature increases up to ~ 7 keV.

Fig. 4 shows the rms amplitude vs. frequency of both

¹ As explained in §1, S_a is an indicator of the state of the source and hence it is usually displayed in the x -axis but here we choose not to follow this convention in order to share both x and y axis for adjacent panels, allowing for a quick comparison between the different relations.

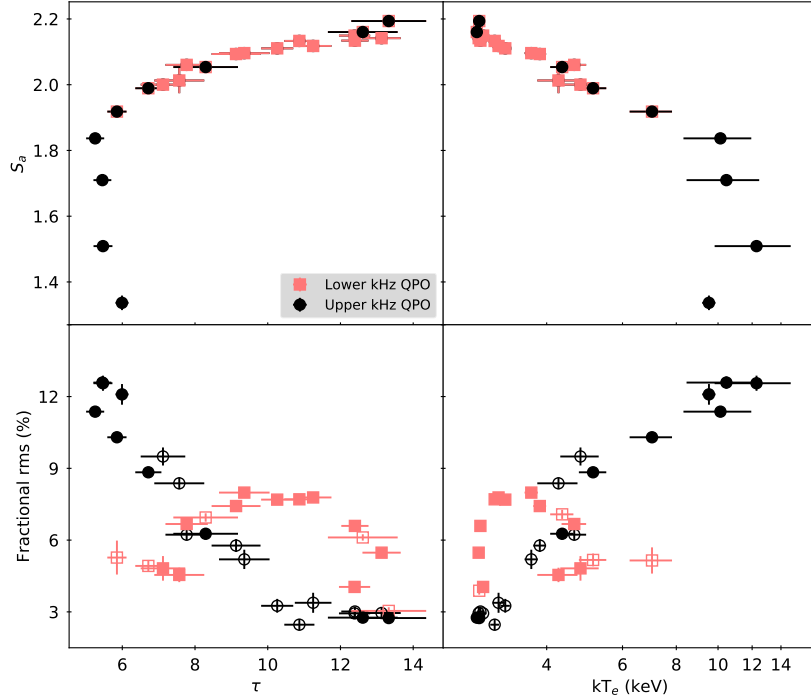


Figure 3. Relations of S_a and fractional rms amplitude as a function of spectral parameters in 4U 1636–53. Symbols are the same as in Fig. 2. The x axis of the right side panels are shown in \log scale for better visualisation. Error bars in rms represent the 1σ confidence interval obtained from the best fit to the combined power spectra. Error bars in the other variables represent the 1σ error of the mean in each bin.

kHz QPO (see, for example, Méndez et al. 2001; Di Salvo et al. 2003; Barret et al. 2005b; Méndez 2006; Altamirano et al. 2008; Boutelier et al. 2010). The amplitude of the upper QPO decreases from approximately 15% to 2% as its frequency increases, with a local maximum ($\sim 11\%$) around 800 Hz, while the amplitude of the lower QPO increases from 4% to 8% as its frequency increases from approximately 500 Hz to 800 Hz and then decreases to 4% as the frequency increases to 950 Hz.

To quantify the local maximum observed in the plot of the rms amplitude vs. frequency for the upper kHz QPO, we first fitted the data points with a linear function (Model 1) and then with a model consisting of a linear function and a Gaussian (Model 2). We give the best fitting parameters in Table 2 and we plot the data and best-fitting models in Fig. 4.

Based on Model 1 we simulated 10^7 datasets with points drawn from a normal distribution with σ equal to the 1σ uncertainties of the rms amplitude at each frequency. We fitted all 10^7 realisations with Model 2 with the FWHM and central frequency of the Gaussian fixed to the best-fitting values, leaving the amplitude of the Gaussian free. From all 10^7 there was no realisation with an amplitude equal or larger than the one we obtained in Model 2, which implies a probability smaller than 10^{-7} that the observed local maximum arises from statistical fluctuations of data that follow a linear relation.

For completeness, and to find the QPO frequency at which the fractional rms amplitude is maximum, we also fitted a Gaussian function to the amplitude of the lower

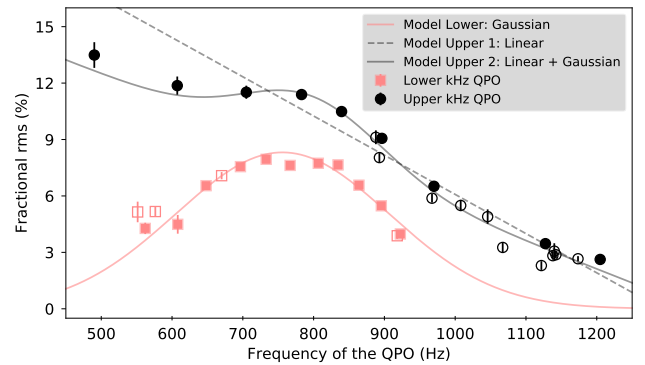


Figure 4. The rms amplitude of the upper and lower kHz QPO in 4U 1636–53 as a function of the QPO frequency. Symbols are the same as in Fig. 2. The dashed-black and solid-black lines show, respectively, the best fitting linear function and linear function plus a Gaussian to the rms amplitude of the upper kHz QPO. The solid-red (grey in the printed version) line shows the best fitting Gaussian function to the rms amplitude of the lower kHz QPO.

kHz QPO. We show the best-fitting parameters in Table 2, and we plot the data and the model in Fig. 4. Our choice of models has no theoretical support and was made simply as a way to quantitatively describe the shape of the rms amplitude of the kHz QPOs as a function of QPO frequency. The errors of the parameters shown in Table 2 are likely

Table 2. Best fitting parameters for the rms amplitude of the kHz QPOs in 4U 1636–53 as a function of the QPO frequency

Upper kHz QPO		
	Model 1 : Linear	Model 2: Linear + Gaussian
Constant term (%)	26.9 ± 0.3	19 ± 1
Slope (% Hz ⁻¹)	-0.0208 ± 0.0003	-0.0148 ± 0.0008
Central frequency (Hz)	–	799 ± 11
FWHM (Hz)	–	229 ± 29
Amplitude (%)	–	3.2 ± 0.3
$\chi^2/d.o.f$	215.5/18	65.6/15
Lower kHz QPO		
	Model: Gaussian	
Central frequency (Hz)	755.9 ± 1.5	
FWHM (Hz)	355 ± 5	
Amplitude (%)	8.32 ± 0.05	
$\chi^2/d.o.f$	202.9/12	

underestimated given that the model is phenomenological and the fits are statistically unacceptable.

4 DISCUSSION

We show that in the NS-LMXB 4U 1636–53 the frequency of the lower and upper kHz QPOs follow the same relation, albeit shifted by ~ 300 Hz from each other, as a function of the spectral parameters of the source, but the fractional amplitude of the lower and upper kHz QPOs follow completely different relations. In the latter case the relation of the rms of one QPO cannot be shifted to obtain the relation of the other.

For frequencies below ~ 400 Hz we do not detect the kHz QPOs, as the PDS of the source starts featuring hectohertz QPOs and broad-band noise components (see [Altamirano et al. 2008](#) for an overview of the X-ray variability in this source). Therefore it is not possible to tell if Figures 2 and 3 represent the whole picture. For example, one might question whether the lower kHz QPO is never present when the temperature kT_e is above 8 keV, or whether it is simply not detected because its frequency would lie in the noisy region of the PDS.

The frequency of the upper kHz QPO is generally associated with the Keplerian motion of matter at the innermost parts of the accretion disc (e.g. [Miller et al. 1998](#); [Stella & Vietri 1998](#); [Lamb & Miller 2001](#); [Török et al. 2016](#)); this idea is consistent with the relation between QPO frequency and S_a , which can be understood in terms of changes in the radius at which the QPO is produced due to changes in mass accretion rate (see §1).

[Fig. 2](#) shows that the dynamical mechanisms that set the frequency of both kHz QPOs are strongly related, or are possibly the same. The frequency of the lower kHz QPO can be shifted to obtain a single relation between the spectral parameters that describe the Comptonising component of the energy spectrum and the kHz QPOs frequencies. Considering that we observe the upper kHz QPO in different spectral states, and the frequencies of both the upper and

lower kHz QPO have the same dependence with spectral parameters, we can argue that, at least dynamically, both kHz QPOs should always be present. The fact that we do not always detect these QPOs in pairs may be due to differences in the radiative mechanisms that set their amplitudes.

In contrast to the behaviour of the frequencies shown in [Fig. 2](#), [Fig. 3](#) shows that the rms fractional amplitude of the upper and lower kHz QPOs have disparate behaviours as a function of spectral parameters. In this case, it is not possible to shift the frequencies or amplitudes of one QPO to obtain the relation shown by the other. The amplitude of the lower kHz QPO shows a maximum for a specific range of values of the spectral parameters and QPO frequency, whereas the amplitude of the upper kHz QPO decreases more or less monotonically with frequency, with a local maximum (seen as a *hump* in [Fig. 4](#)) at ~ 800 Hz. Therefore the radiative mechanisms that sets the amplitude of, respectively, the lower and the upper kHz QPO are likely different. It is interesting to notice that the energy and frequency dependence of the time lags of the kHz QPOs in 4U 1636–53 also suggest two different radiative mechanisms responsible for each QPO ([De Avellar et al. 2013](#)).

As [Zhang et al. \(2017\)](#) pointed out, at ~ 850 Hz the lower kHz is more often detected and has its highest quality factor ([Belloni et al. 2005](#); [Barret et al. 2006](#)); this is also the frequency at which the phase lags of the lower kHz QPO are the largest and the coherence between low- and high-energy signals is the highest ([De Avellar et al. 2013, 2016](#)). All these phenomena happening over a relatively narrow range of frequencies, and specific spectral parameters, suggest that a resonance mechanism may drive the amplitude of the lower kHz QPO.

We fitted the rms amplitude of both kHz QPO in order to describe the shape of the rms as a function of the QPO frequency. We find that the local maximum of the amplitude of the upper kHz QPOs and the global maximum of the amplitude of the lower kHz QPO occur respectively at ~ 800 Hz and ~ 760 Hz. Those values were obtained by fitting simple mathematical models to the rms amplitude and they represent the central values of broad features of the rms-frequency relation.

While this may only be a coincidence, it is curious that the peaks of these features are at similar frequencies. (Notice that the spectral properties of the source are different when the lower kHz QPO is at 800 Hz than when the upper kHz QPO is at that same frequency.) It could be that a specific combination of spectral parameters (and size, which we do not measure in this work) of the corona triggers (or amplifies) the coupling between disc and corona. One possible scenario is that there is a radiative mechanism that sets the rms amplitude of both QPOs, which peaks at ~ 800 Hz, whereas there is another mechanism that acts only upon the upper kHz QPO and drives the more or less linear decay of its rms with frequency. (Notice that this does not necessarily implies that the QPO frequency drives the rms amplitude, but the rms amplitude could also be determined by the spectral properties of the source.)

The amplitude of both kHz QPOs increases with photon energy (e.g., [Berger et al. 1996](#); [Wijnands et al. 1997](#); [Méndez et al. 2001](#); [Gilfanov et al. 2003](#)); together with our results this reinforces the notion that even if the oscillations are driven by the dynamics of matter at particular radii in

the accretion disc, as for example at the innermost stable circular orbit (e.g. Miller et al. 1998; Lamb & Miller 2001; Barret et al. 2005a,b, 2006, 2007), the amplitudes of the QPOs are driven by changes in the spectral component that is responsible for the high energy emission in the energy spectrum. Another possibility is that the oscillations arise from the high-energy component itself (Lee et al. 2001; see also Kumar & Misra 2014), where the Comptonising plasma oscillates at the lower kHz QPO frequency or, as proposed by Gilfanov et al. (2003), the QPOs reflect oscillations in a Comptonised boundary layer.

Our results support the idea that the properties of the kHz QPOs are the outcome of a complex interplay between the dynamics of matter around the neutron star, and the radiative processes and the interactions between the accretion disc, the neutron star surface, and the Comptonising region. The fact that frequency and amplitude of the kHz QPO have different behaviours in relation to the spectral parameters should be inherent to any physical model proposed to describe the mechanisms that produce each of the kHz QPOs in 4U 1636–53, and possibly other sources.

A key step to understand the nature of the mechanism behind the kHz QPOs in NS-LMXB is the combined use of spectral and timing techniques to find the link between the timing properties and the physical state of the systems. We gave here the first steps in this direction by comparing the properties of the kHz QPO and the parameters that describe the Comptonising region on 4U 1636–53. Our results should help the development of models that would allow us to describe the physical properties of the Comptonising region, the neutron star itself, and the accretion flow around it, by using the timing properties of the kHz QPO.

ACKNOWLEDGEMENTS

The authors are grateful to the anonymous referee for contributing to the improvement of this paper. E.M.R acknowledges the support from Conselho Nacional de Desenvolvimento Científico e Tecnológico (CNPq - Brazil). This research has made use of data obtained from the High Energy Astrophysics Science Archive Research Center (HEASARC), provided by NASA's Goddard Space Flight Center

REFERENCES

Altamirano D., van der Klis M., Méndez M., Jonker P. G., Klein-Wolt M., Lewin W. H. G., 2008, *ApJ*, 685, 436
 Anders E., Grevesse N., 1989, *Geochimica Cosmochimica Acta*, 53, 197
 Arnaud K., 1996, *Astronomical Data Analysis Software and Systems V*, 101, 17
 Balucinska-Church M., McCammon D., 1992, *ApJ*, 400, 699
 Barret D., Olive J.-F., Miller M. C., 2005a, *Astron. Nachr.*, 326, 808
 Barret D., Olive J.-F., Miller M. C., 2005b, *MNRAS*, 361, 855
 Barret D., Olive J. F., Miller M. C., 2006, *MNRAS*, 370, 1140
 Barret D., Olive J. F., Miller M. C., 2007, *MNRAS*, 376, 1139
 Belloni T., Méndez M., Homan J., 2005, *A&A*, 437, 209
 Belloni T. M., Homan J., Motta S., Ratti E., Méndez M., 2007, *MNRAS*, 379, 247
 Berger M., et al., 1996, *ApJ*, 469, L13

Boutelier M., Barret D., Lin Y., Török G., 2010, *MNRAS*, 401, 1290
 De Avellar M. G. B., Méndez M., Sanna A., Horvath J. E., 2013, *MNRAS*, 433, 3453
 De Avellar M. G. B., Méndez M., Altamirano D., Sanna A., Zhang G., 2016, *MNRAS*, 461, 79
 Di Salvo T., Méndez M., van der Klis M., Ford E., Robba N. R., 2001, *ApJ*, 546, 1107
 Di Salvo T., Méndez M., van der Klis M., 2003, *A&A*, 192, 17
 Done C., Gierliński M., Kubota A., 2007, *A&ARv*, 15, 1
 Ford E. C., van der Klis M., Méndez M., Wijnands R., Homan J., Jonker P. G., van Paradijs J., 2000, *ApJ*, 537, 368
 Gilfanov M., Revnivtsev M., Molkov S., 2003, *A&A*, 410, 217
 Hasinger G., van der Klis M., 1989, *A&A*, 225, 79
 Jahoda K., Markwardt C. B., Radeva Y., Rots A. H., Stark M. J., Swank J. H., Strohmayer T. E., Zhang W., 2006, *ApJS*, 163, 401
 Jonker P. G., Wijnands R., van der Klis M., Psaltis D., Kuulkers E., Lamb F. K., 1998, *ApJ*, 499, L191
 Jonker P. G., Méndez M., van der Klis M., 2002, *MNRAS*, 336, 1996
 Kumar N., Misra R., 2014, *MNRAS*, 445, 2818
 Kuulkers E., van der Klis M., Oosterbroek T., Asai K., Dotani T., van Paradijs J., Lewin W. H. G., 1994, *A&A*, 289, 795
 Lamb F. K., Miller M. C., 2001, *ApJ*, 554, 1210
 Lee H. C., Misra R., Taam R. E., 2001, *ApJ*, 549, L229
 Makishima K., Maejima Y., Mitsuda K., Bradt H. V., Remillard R. A., Tuohy I. R., Hoshi R., Nakagawa M., 1986, *ApJ*, 308, 635
 Méndez M., 2006, *MNRAS*, 371, 1925
 Méndez M., et al., 1998, *ApJ*, 494, L65
 Méndez M., van der Klis M., Ford E. C., Wijnands R. a. D., van Paradijs J., 1999, *ApJ*, 511, L49
 Méndez M., van der Klis M., Ford E. C., 2001, *ApJ*, 561, 1016
 Miller M. C., Lamb F. K., Psaltis D., 1998, *ApJ*, 508, 791
 Mitsuda K., et al., 1984, *PASJ*, 36, 741
 Rothschild R. E., et al., 1998, *ApJ*, 496, 538
 Sanna A., Méndez M., Belloni T. M., Altamirano D., 2012, *MNRAS*, 424, 2936
 Sanna A., Hiemstra B., Méndez M., Altamirano D., Belloni T., Linares M., 2013, *MNRAS*, 432, 1144
 Shih I. C., Bird A. J., Charles P. A., Cornelisse R., Tiramani D., 2005, *MNRAS*, 361, 602
 Stella L., Vietri M., 1998, *ApJ*, 492, L59
 Sunyaev R. a., Titarchuk L. G., 1980, *A&A*, 86, 121
 Török G., Goluchová K., Horák J., Šrámková E., Urbanec M., Pecháček T., Bakala P., 2016, *MNRAS*, 457, L19
 Van Paradijs J., et al., 1990, *A&A*, 234, 181
 Van Straaten S., Ford E. C., van der Klis M., Méndez M., Kaaret P., 2000, *ApJ*, 540, 1049
 Wijnands R. A. D., van der Klis M., van Paradijs J., Lewin W. H. G., Lamb F. K., Vaughan B., Kuulkers E., 1997, *ApJ*, 479, L141
 Zdziarski A. A., Johnson W. N., Magdziarz P., 1996, *MNRAS*, 283, 193
 Zhang W., Lapidus I., Swank J. H., White N. E., Titarchuk L., 1997, *IAU Circ.*, 6541
 Zhang G., Méndez M., Sanna A., Ribeiro E. M., Gelfand J. D., 2017, *MNRAS*, 465, 5003
 Życki P. T., Done C., Smith D. A., 1999, *MNRAS*, 309, 561